Scilight

Photochemistry and Spectroscopy
https://www.sciltp.com/journals/ps

Article

Defect-Engineering in MoS_2 Layers for Surface Enhanced Raman Scattering

Antonio Brancato [1], Marcello Condorelli [1,2,*], Vittorio Scardaci [1], Enza Fazio [3], Giuseppe Forte [4], Luisa D'Urso [1] and Giuseppe Compagnini [1,2]

[1] Department of Chemical Sciences, University of Catania, 95125 Catania, Italy
[2] Istituto Nazionale Scienza e Tecnologia dei Materiali (INSTM), 95124 Catani, Italy
[3] Department of Mathematical and Computer Science, Physical Science and Earth Science (MIFT) 31, 98166 Messina, Italy
[4] Department of Drug and Health Sciences, University of Catania, 95125 Catania, Italy
* Correspondence: marcello.condorelli@unict.it

How To Cite: Brancato, A.; Condorelli, M.; Scardaci, V.; et al. Defect-Engineering in MoS_2 Layers for Surface Enhanced Raman Scattering. *Photochemistry and Spectroscopy* **2026**, *2*(1), 5. https://doi.org/10.53941/ps.2026.100005

Received: 3 November 2025
Revised: 5 December 2025
Accepted: 9 December 2025
Published: 29 January 2026

Abstract: Surface-enhanced Raman scattering (SERS) offers exceptional molecular sensitivity, but the instability and poor reproducibility of noble metal substrates limit its practical use. Here, we investigate low-cost, non-plasmonic alternatives based on two-dimensional molybdenum disulfide (MoS_2). We introduce a reagent-free, pulsed-laser irradiation in liquid protocol to controllably engineer defects and induce the metallic 1T phase within MoS_2, thereby tailoring its electronic structure through sulfur vacancies. Laser-modified MoS_2 displays markedly enhanced SERS activity relative to unmodified 2H-MoS_2; the enhancement correlates with increased density of defect sites and the presence of the conducting 1T phase, which together promote more efficient substrate-adsorbate charge transfer. By using 4-mercaptobenzoic acid (4-MBA) as a probe molecule, laser-modified MoS_2 shows a SERS enhancement factor of $\approx 10^5$ compared with pristine 2H-MoS_2 under 532 nm excitation. The experimental results were further validated by density functional theory calculations, which show a better match of the energy level of MoS_2 1T with our probe molecule, supporting the ongoing research aimed at designing novel SERS substrates. Our results demonstrate that phase and defect engineering in 2D materials provide a robust route to reproducible, non-plasmonic SERS substrates, offering a scalable alternative to noble metals for sensitive chemical and biosensing applications.

Keywords: nanomaterials; defect engineering; Raman scattering; SERS; laser modification

1. Introduction

Surface-enhanced Raman scattering (SERS) is a highly sensitive, molecule-specific spectroscopic technique that can reach single-molecule detection in optimal conditions [1]. Despite its sensitivity, widespread application of SERS in quantitative and real-world applications is limited by reproducibility and stability issues, particularly for conventional noble-metal substrates. Silver and gold nanostructures provide large electromagnetic (EM) enhancement via localized surface plasmon resonances, but they are prone to chemical degradation (e.g., silver oxidation and carbon contamination), uncontrolled aggregation in colloidal media, and high material costs [2]. These drawbacks motivate the development of alternative SERS platforms that maintain strong enhancement while improving robustness and reproducibility [3]. Metal-free or low-cost plasmonic alternatives and semiconductor substrates are promising stable and easily scalable SERS substrates [4]. Transition-metal nitrides (e.g., TiN) can display plasmonic-like behavior at reduced cost [5], while oxide and chalcogenide semiconductors (for example,

TiO_2, ZnO, and MoS_2) offer superior chemical and structural stability [6]. Importantly, chalcogenides contribute to SERS predominantly through a chemical enhancement mechanism (CM) rather than by classical EM amplification [7]. Chemical enhancement originates from photoinduced electronic interactions at the substrate adsorbate interface. In detail, when the electronic levels of substrate and molecule are favourably aligned, light can drive interfacial charge transfer that transiently modifies the adsorbate polarizability and increases its Raman cross section, enhancing the signal's intensity [8]. Examples of this phenomenon include electron transfer from the semiconductor valence band to a molecule's LUMO or from a molecule's HOMO to the semiconductor conduction band [6]. Consequently, the efficiency of chemical enhancement strongly depends on the electronic band structure of the semiconductor; introducing atomic defects, such as vacancy point defects (e.g., vacancies), heteroatom doping, or phase transitions, can, therefore, create in-gap states that facilitate charge transfer [9]. For example, antimony-doped tin oxide nanoparticles show a band gap modulation correlated with carrier density, leading to enhanced SERS activity. An optimal Sb doping level of 1.5% was identified for maximizing SERS enhancement [10]. For these reasons, defect engineering and phase control are the most promising strategies to tune semiconductor electronic structure for SERS. In this context, two-dimensional transition-metal dichalcogenides (TMDs), notably MoS_2, are particularly attractive because their electronic properties can be tuned by controlling phase (semiconducting 2H versus metallic 1T/1T′) and defect density [11]. Metallic phases and defect-rich TMDs may also support surface states that yield emergent EM-like effects, enabling a hybrid chemical and EM enhancement without noble metals [12].

In this work, pulsed laser irradiation in liquids (PLIL) is used as a rapid, reagent-free technique to engineer the MoS_2 phase and defect. Short laser pulses applied to colloidal dispersions produce localized heating and photochemical effects that can fragment particles, induce phase transformations, and generate high densities of vacancies and reduced-valence centers [13]. Moreover, PLIL is scalable, performed in green solvents, and allows tuning of defect density and phase composition through laser parameters and solvent selection [14]. We characterize laser-induced changes using complementary morphological, structural, and surface-sensitive techniques (Trasmission Electron Microscopy (TEM), Raman spectroscopy, X-ray photoelectron spectroscopy (XPS), and optical absorption) to correlate structural/chemical modifications with electronic properties. SERS activity of the engineered material is evaluated using 4-mercaptobenzoic acid (4-MBA) as a probe and compared directly with pristine MoS_2. The novelty of this study lies in the controlled application of PLIL to simultaneously tailor defects and phase modifications in MoS_2 dispersions to enhance interfacial charge-transfer channels responsible for chemical SERS enhancement, while avoiding common drawbacks of noble-metal substrates (oxidation, aggregation, expensiveness). Applying the method of density functional theory (DFT) calculations, we examine the role of the 2H-MoS_2, 1T-MoS_2 and sulfur vacancies on the analyte adsorption and therefore on the charge transfer phenomena between the probe molecule and the SERS active substrate. DFT provided a reliable and accurate analysis of the molecule-surface chemical coupling in SERS, assigning distinct roles to the induced chemical modifications in their contribution to signal amplification through chemical mechanisms.

This study demonstrates that PLIL can effectively modulate the charge-transfer efficiency of semiconductor-based SERS substrates, offering a sustainable, flexible, and scalable approach for developing reproducible, uniform and noble metal-free platforms based on defect- and phase-engineered 2D materials.

2. Experimentals

Laser modification of MoS_2 was carried out by irradiating 3 mL of a commercial (Graphene Supermarket) dispersion of MoS_2 nanoflakes (18 mg/L) in a water (45% vol.)/ethanol (55% vol.) mixture. Different timeframes, in a range 0–15 min, are used to induce structural changes and defects in the raw material, by using an unfocused pulsed Nd:YAG laser (Continuum, Surelite II model Nd:YAG laser, pulse duration = 5 ns, repetition rate = 10 Hz). The second harmonic of the laser (532 nm) was employed to irradiate MoS_2 sheets, with an output power of 1.1 W (fluence ~0.39 J/cm^2), a repetition rate of 10 Hz, and a pulse duration of approximately 5 ns. The laser was unfocused on the dispersion with a beam diameter of 6 mm. The dispersion was stirred during laser irradiation to prevent sedimentation of the new structures formed. After laser irradiation, modified 2D structures were collected by centrifugation (8000 r.p.m. for 5 min) and washed several times with the deionized water and dispersed in a water (45%)/ethanol (55%) mixture. The pristine and the laser-modified MoS_2 dispersions were optically characterized by UV-Vis absorption and photoluminescence (PL) spectroscopies. Absorption spectra were recorded in the 200–1000 nm range using an Agilent Cary 60 UV-Vis spectrophotometer (Agilent, Via P. Gobetti 2/C 20063 Cernusco sul Naviglio Milano, Italy), while PL analyses were performed by a HORIBA Fluoromax spectrofluorometer (HORIBA,Viale Luca Gaurico 209/211, Roma, Italy), acquiring the emission spectra at an excitation wavelength of λ_{exc} = 532 nm. Morphological investigations were carried out through TEM, STEM. For

TEM characterization, 5 µL of the MoS_2 dispersion (pristine and irradiated) were deposited on a copper grid and dried for 12 h before to acquire images. TEM analyses were conducted on a Zeiss 900 N instrument (Carl Zeiss Microscopy GmbH, Jena, Germania) operated at 80 kV. STEM images were obtained with a ZEISS Merlin Gemini 2 microscope (Carl Zeiss Microscopy GmbH, Jena, Germania) operated at 30 kV, in this case a drop of the MoS_2 irradiated dispersion was deposited on a silicon substrate. Phase changes in MoS_2 were examined by Raman spectroscopy, employing an excitation wavelength of 532 nm of a Sapphire Laser (Coherent Inc., Santa Clara, CA, USA) mounted on a WITec alpha 300 (Wissenschaftliche Instrumente und Technologie GmbH, Ulm, Germany) confocal Raman apparatus. The laser power was set at 0.5 mW to avoid potential alteration of the samples. Spectra have been collected by a 10× objective, an integration time of 10 s per spectrum and 10 accumulations on the dispersions deposited on HOPG and silicon substrates.

Elemental speciation was investigated by XPS using a Thermo Fisher ESCALAB 250Xi (Thermo Fisher, Waltham, MA, USA) equipped with monochromatic Al Kα radiation and argon-assisted charge compensation. Spectra were averaged over 10 scans with a pass energy of 10 eV, a step size of 0.05 eV, and a dwell time of 100 ms. In this case 10 µL of the investigated samples were deposited on a Silicon substrate and air-dried for 12 h.

Finally, SERS samples were prepared by mixing ethanolic solutions of 4-MBA (in a concentration range of 10^{-3}–10^{-6} M) with MoS_2 dispersions for 24 h allowing the adsorption of the molecules onto the MoS_2 platforms. The mixtures were centrifuged (8000 r.p.m., t = 5 min) to remove the supernatant and the unbound molecules and then re-dispersed in water. Then a drop of the dispersions was deposited onto silicon wafers and after the complete water evaporation, single spectra SERS measurements were performed by acquiring signals at a laser power of 0.5 mW with an acquisition time of 10 sec and 10 accumulation per spectrum. Imaging maps were obtained by scanning a 15 × 15 μm^2 area of the sample with a 532 nm laser using a 100× objective. The scanned area was divided into 10,000 pixels, and one SERS spectrum was collected from each pixel with an acquisition time of 0.01 s and 10 accumulations per spectrum. For each scanned pixel, the intensity of the strongest SERS signal of 4-MBA at 1594 cm^{-1} was recorded, producing an intensity map in false colours that visualizes the signal distribution across the scanned area. A scheme of the overall experimental procedure to obtain defective MoS_2 architectures is reported in Figure 1.

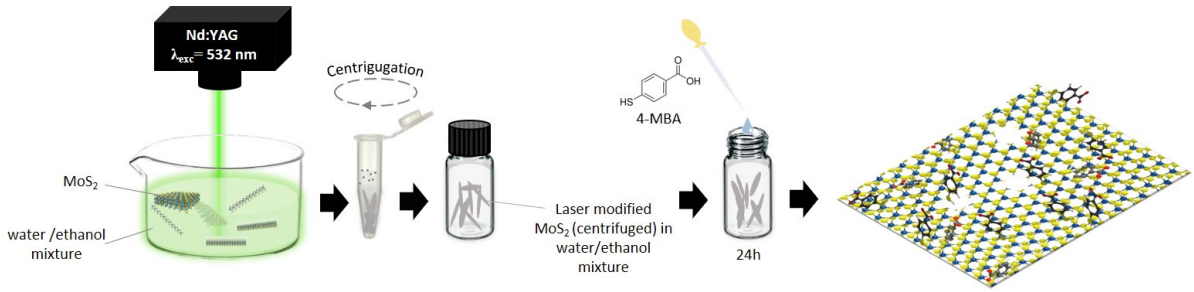

Figure 1. Experimental Scheme of preparation of defective MoS_2- based SERS substrates.

3. Computational Methods

All density functional theory (DFT) calculations were carried out using the Vienna Ab-initio Simulation Package (VASP, version 6.5.1) [15]. The projector-augmented wave (PAW) method was employed to describe the electron–ion interaction [16]. Exchange–correlation effects were treated within the generalized gradient approximation (GGA) using the Perdew–Burke–Ernzerhof (PBE) functional [17]. Dispersion corrections were included through the nonlocal van der Waals (vdW-DF) functional when required [18,19]. Three MoS_2 configurations were investigated, (i) the pristine semiconducting 2H phase, (ii) the metallic 1T phase and (iii) a S-vacancy-defective 2H-MoS_2 (one sulfur vacancy per 4 × 4 supercell). Each slab was modeled as a monolayer of MoS_2 with a vacuum spacing of at least 20 Å along the z-direction to prevent spurious interactions between periodic images. The adsorbate molecule, 4-mercaptobenzoic acid (4-MBA), was initially optimized in a 20 × 20 × 20 $Å^3$ box under periodic boundary conditions. Adsorption configurations were prepared by placing the molecule above the MoS_2 surface either on a metallic 1T (Figure S1a), or a S-vacancy site (Figure S1b). A plane-wave cutoff energy of 520 eV was set, together with an energy convergence value of 10^{-6} eV. For surface models, Brillouin-zone integrations were performed using a Γ-centered k-point grid of (5 × 5 × 1) for 4 × 4 supercells. The band edges (VBM, CBM, or EFermi for metallic systems) of MoS_2 phases were aligned to vacuum using the average vacuum potential from LOCPOT files. Projected DOS were extracted from vasprun.xml files integrating orbital

contributions of Mo, S, and C, O, S atoms. Energy references were shifted so that the Fermi level is at 0 eV for each system. Finally, charge-density differences were computed as [20]:

$$\Delta\rho = \rho(\text{adsorbate + slab}) - \rho(\text{slab}) - \rho(\text{adsorbate})$$

using identical grid parameters across all systems.

4. Results and Discussion

Figure 2 shows TEM images representing three different irradiation times modifying MoS_2 together with the starting MoS_2: (a) pristine MoS_2 (t = 0), (b) t = 5 min, (c) t = 10 min and (d) t = 15 min. All analysed samples were irradiated with a laser wavelength of 532 nm at a power of 1.1 W. The TEM images distinctly reveal the morphological changes; the pristine MoS_2 dispersion consists of nanoflakes with lateral dimensions of a few hundred nanometers (Figure 2a), after 5 min of irradiation, elongated structures of approximately 300 nm become well visible (Figure 2b), which further grow after 10 min (Figure 2c), reaching micrometric or larger dimensions after 15 min (Figure 2d).

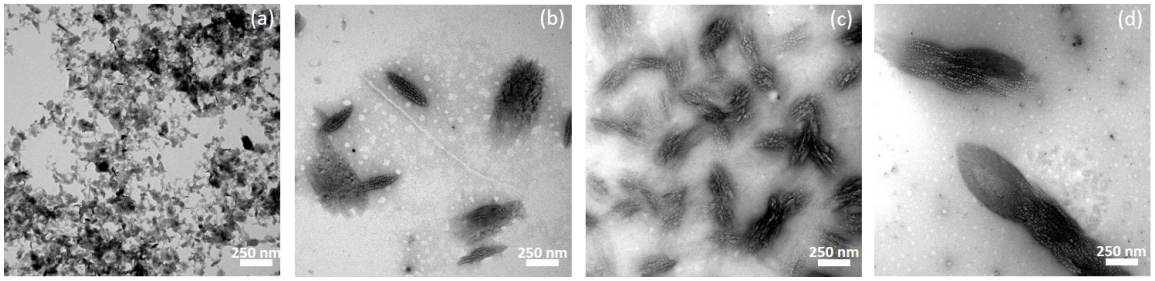

Figure 2. TEM images of (**a**) Pristine MoS_2 (t = 0), (**b**) after 5 min, (**c**) 10 min and (**d**) 15 min of laser irradiation.

The TEM observations suggest that laser irradiation can induce either the coalescence of MoS_2 nanoflakes and/or a self-assembly process. In general, pulsed laser irradiation can generate stress conditions high enough to promote defect formation or even melting of the material. For example, Luo et al. reported similar melting and assembly phenomena in MoS_2 nanoflakes under nanosecond green laser irradiation, leading to the formation of fullerene-like structures [21,22]. The appearance of these fullerene-like structures is attributed to defect formation and the system's tendency to minimize surface energy by reorganizing the MoS_2 sheets into new geometries. In our case, however, the irradiation conditions are milder, and we do not observe the formation of fullerene-like structures, but rather a simple linear assembly of the MoS_2 sheets. A similar outcome was reported by Ibrahim et al., who studied the reorganization of 2D materials under femtosecond pulsed laser irradiation at a wavelength of 800 nm (non-resonant with MoS_2 absorption bands). They employed a polarized, focused beam directly applied to the dispersion and attributed the self-organization to the strong electric field at the laser focus. This field fragmented the MoS_2 nanoflakes into smaller particles, which then aligned according to the light polarization [23]. In contrast, the current study employed an unfocused nanosecond laser, leading to a less vigorous process. However, the irradiation wavelength of 532 nm corresponds to one of MoS_2 absorption bands, suggesting that electronic excitation and non-radiative relaxation mechanisms could induce localized heating, promoting coalescence. To further investigate the organization of the elongated microstructures, STEM images (Figure 3a,b) at different magnifications, were obtained for the sample irradiated for 15 min. These analyses revealed significant surface nanoroughness, which may have originated from the assembly of the initial MoS_2 flakes in random orientations.

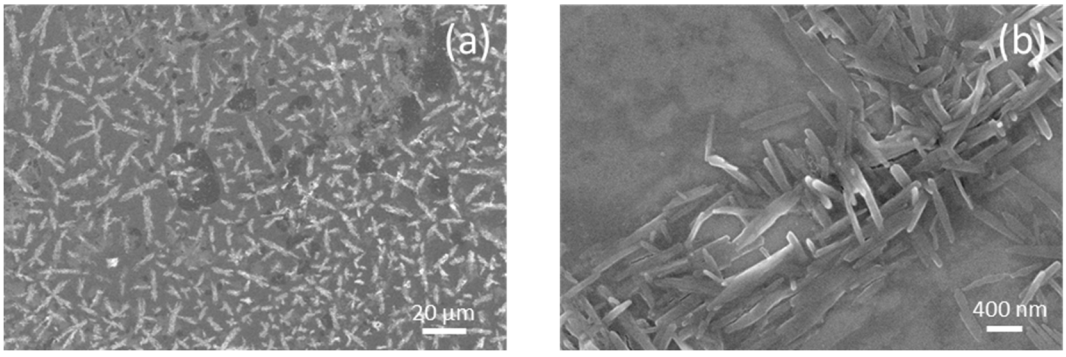

Figure 3. STEM images of MoS_2 laser-modified after 15 min of irradiation time (**a**) low magnification (**b**) High magnification.

To further investigate the growth process and study the changes in the optical properties of MoS_2, UV-Vis absorption spectra (Figure 4a) were recorded for the dispersion after irradiation times (t_{irr}) of 0, 5, 10, and 15 min. Upon analyzing the UV-Vis spectra, it is clear that, before laser exposure, the sample exhibits substantial absorption in the range of 200 nm to 700 nm, characterized by several electronic transitions. Two prominent bands are observed at 603 nm and 662 nm (typically denoted as B and A, respectively), which are associated with excitonic transitions at the K point of the Brillouin zone [24]. In addition, the absorption bands between 200 nm and 500 nm are attributed to direct transitions from the deep valence band to the conduction band, conventionally labeled as transitions C, D, and E [25]. The overall absorption spectrum of starting MoS_2 reflects the characteristic electronic structure of two-dimensional transition metal dichalcogenides, from which valuable information regarding the number of stacking layers can be inferred through the behaviour of the A excitonic transition. For instance, Castellanos-Gomez et al. demonstrated that the A excitonic peak undergoes a redshift proportional to the increasing number of MoS_2 layers [25]. In the spectrum of the non-irradiated sample, the position of the A excitonic band suggests the presence of few-layer MoS_2 (ranging from 2 to approximately 7 layers, as indicated by the commercial dispersion specifications). During the laser modification process, the appearance of the MoS_2 dispersion gradually transitioned from pale yellow to nearly transparent. Concurrently, the absorption spectra exhibited significant changes with increasing irradiation time, showing a pronounced absorption band between 200 and 300 nm, while the visible excitonic transitions diminished drastically and nearly disappeared, indicating a significant reorganization of the electronic structure. The newly observed ultraviolet absorption band stabilized after approximately 10 min of irradiation, suggesting substantial alterations in the chemical structure of MoS_2 due to the pulsed-laser interaction. Absorption features within the same spectral region have previously been associated with both molybdenum oxide species [26] and sulfur vacancy formation, as well as with a phase transition from the semiconducting 2H phase to the metallic 1T phase [27].

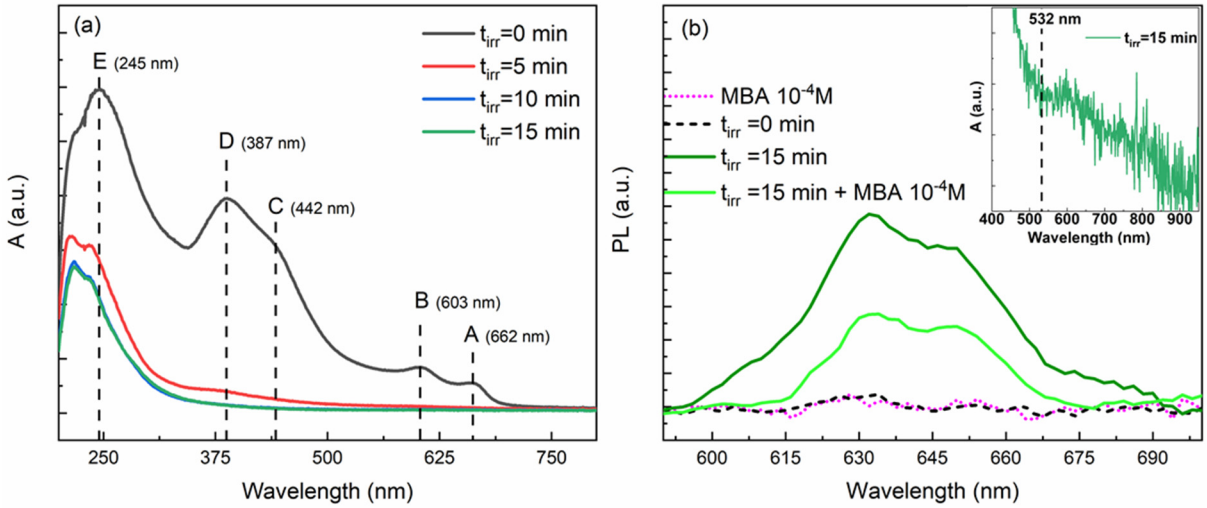

Figure 4. UV-Vis spectra evolution of MoS_2 dispersion during 15 min of laser irradiation (**a**,**b**) photoluminescence spectra under 532 nm excitation of the pristine sample (t_{irr} = 0, dashed black line), MoS_2 at t_{irr} = 15 min (dark green line) and in presence of 4-MBA 10^{-4} M (light green line) and of 4-MBA 10^{-4} M (pink line).

In order to deeply understand charge transfer phenomena, it was useful to investigate possible variations in the photoluminescence (PL) response of the sample in the presence of the analyte. Thus, photoluminescence measurements were performed by exciting the samples with a 532 nm laser line, corresponding to the excitation wavelength used in SERS experiments.

In the inset of Figure 4b the UV-Vis absorption tail of the sample irradiated for 15 min is shown. Although weak, a measurable absorption is observed at 532 nm. Figure 4b presents the PL spectra recorded under 532 nm excitation for the pristine sample (t_{irr} = 0, dashed black line), the laser-modified sample (t_{irr} = 15 min, dark green line), and the same sample interacting with the probe molecule at a concentration of 10^{-4} M (light green line). For comparison the 4-MBA PL spectrum it is also shown (pink line).

The non-irradiated sample shows no detectable photoluminescence, indicating that multiple pristine layers are stacked together, resulting in an indirect bandgap that quenches the emission typically observed in monolayer samples, where the bandgap is direct [28]. This quenching arises from interlayer interactions which become increasingly significant with the addition of layers, causing a distortion in the band structure and shifting the conduction band minimum and valence band maximum to different points in k-space [28].

In contrast, the sample irradiated for 15 min exhibits a weak photoluminescence band in the 600–700 nm range. Although this wavelength region corresponds to the emission of direct-bandgap MoS_2, the origin of this feature is not easy to determine. We suggest that the introduction of oxygen defects and sulfur vacancies generates new electronic states which facilitate, weakly, radiative recombination processes.

The most interesting aspect is the quenching of photoluminescence upon the addition of MBA at concentrations 10^{-4} M suggesting that the interaction between laser-modified MoS_2 and MBA inhibits radiative charge-carrier recombination, indicating the possible charge-transfer processes. We excluded dilution effects since the analyte was added from a 10^{-1} M stock solution, ensuring that the additional volume was negligible.

We hypothesize that the MBA molecule creates new electronic states that are not localized on MoS_2. These additional states allow charge carriers to populate intermediate levels associated with MBA during the decay, thereby partly suppressing radiative recombination on the electronic states localized on MoS_2. For example, Khan et al. reported that the interaction between MoS_2 and diindenoperylene molecules results in a pronounced photoluminescence quenching, which was attributed to the formation of trap states that suppress electron transfer from the LUMO of diindenoperylene to the conduction band minima of MoS_2 [29].

To investigate phase transitions and oxide formation, Raman spectra were recorded on MoS_2 samples as a function of irradiation time (0, 5, 10, and 15 min), as shown in Figure 5a. The spectrum of the non-irradiated sample exhibits two dominant peaks at 382.7 cm^{-1} and 406.9 cm^{-1}, corresponding to the in-plane (E_{2g}) and out-of-plane (A_{1g}) S-Mo-S vibrational modes, respectively. These features are characteristic of 2D MoS_2, and the observed ~24 cm^{-1} separation between the two modes indicates that the MoS_2 flakes consist of multilayer stacks [30].

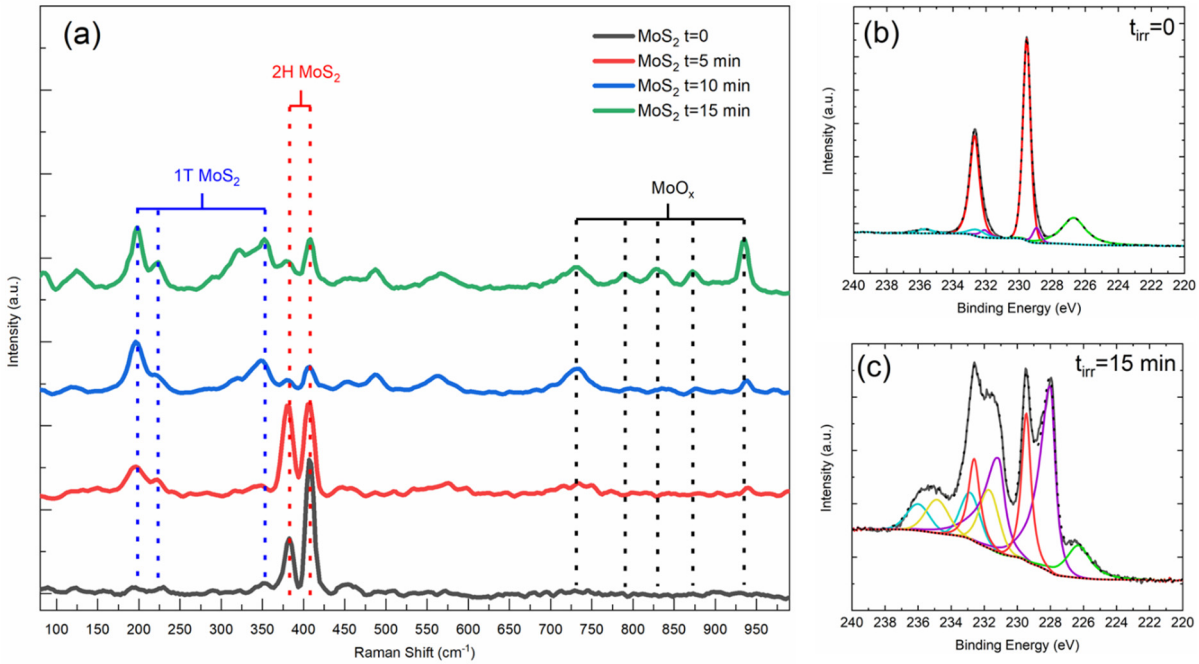

Figure 5. Raman spectra vs irradiation time (**a**) XPS spectra of Mo3d region of (**b**) pristine and (**c**) 15 min laser-modified samples.

After 5 min of pulsed-laser irradiation, the samples still display the E_{2g} and A_{2g} modes as the main features; however, the intensity ratio of A_{1g}/E_{2g} decreases, suggesting that the MoS_2 domains tend to reorganize into a more horizontal arrangement [31]. This observation is consistent with the TEM images, which show the formation of planar structures. Furthermore, after 10 min of irradiation, new Raman bands appear at 197, 222, and 352 cm^{-1}, which indicate a partial phase transition from the semiconducting 2H-MoS_2 to the more metallic 1T-MoS_2 phase, as previously reported by [32]. These results support the hypotheses derived from the UV-Vis absorption and XPS spectra. Additionally, several new features emerge in the 700–950 cm^{-1} region, which can be attributed to the formation of mixed molybdenum oxides [33]. These bands become more pronounced after 15 min of irradiation, in agreement with the XPS results.

To investigate potential atomic defects involving molybdenum and sulfur and to validate the Raman observations regarding the Mo oxidation state, precise determination of the stoichiometry of the irradiated samples is essential for correlating the composition with the enhanced properties observed in SERS experiments. Therefore, XPS analyses were carried out on the original MoS_2 dispersion and on the 15 min irradiated sample in the Mo3d

region. Figure 5b presents the XPS spectrum of the pristine MoS_2 sample, which is characterized by two spin-orbit split components centered at binding energies of 229.56 eV and 232.69 eV, typical of molybdenum atoms bonded to sulfur in 2D MoS_2 structures [34]. Additionally, a third signal corresponding to the sulfur 2 s core level is observed at 226.72 eV, slightly overlapping with the Mo signals, further confirming the presence of MoS_2. The XPS spectrum of the laser-modified sample, irradiated for 15 min (Figure 5c), exhibits significant differences compared to the pristine material, indicating that molybdenum underwent chemical transformations involving changes in oxidation states and bonding configurations. Specifically, after laser irradiation, three well resolved Mo $3d_{5/2}$–$3d_{3/2}$ doublets (attributable to three valence states of molybdenum) were observed in the XPS Mo 3d spectrum. The Mo 3d spectrum shows a main doublet at 229.4 eV ($3d_{5/2}$) and 232.5 eV ($3d_{3/2}$), which is characteristic of Mo^{4+} in MoS_2. Additional Mo $3d_{5/2}$–$3d_{3/2}$ doublets appear at 231.7–234.85 eV, consistent with Mo^{5+} species, and at 232.7–235.8 eV, which are typical of Mo^{6+}. These higher-binding-energy components indicate the presence of oxidized molybdenum states in the laser-modified sample [35]. The shift of Mo species and the tailoring of the peak, at about 228.0 eV, of metallic-like molybdenum (Mo) species could arise from sulfur vacancies, forming sulfur-deficient MoS_{2-x} and/or ascribed to a structural phase transition from the MoS_2 semiconducting 2H phase to the metallic 1T one [36,37]. The laser treatment causes changes in the MoS_2 sample either by introducing sulfur vacancies or by triggering a phase change, both of which make the material more metallic rather than semiconducting. This is also supported by the quantitative analysis. For the laser-modified sample, the integrated peak areas at 232.90 eV, 236.04 eV, 231.70 eV, and 234.85 eV constitute 28.4% of the total Mo 3d spectral intensity and are attributed to mixed molybdenum oxide phases generated via laser irradiation. The peaks centered at 228.04 eV and 231.21 eV represent the predominant component, accounting for 48.7% of the Mo 3d signal, which is ascribed to the formation of sulfur vacancies within the MoS_2 lattice. The residual peaks at 229.45 eV and 232.66 eV comprise 22.9% of the spectrum and correlate with pristine MoS_2, indicating that the laser treatment led to substantial modification in the molybdenum chemical state distribution. XPS studies show that defect creation, including metallic Mo formation, relates to sulfur vacancies, with lower binding energy features reflecting increased defect density and metallic character enhancing surface reactivity. These defects modify the electronic structure of MoS_2, improving charge transfer, electron mobility, and molecular interactions at the surface. This, in turn, increases the polarizability of the adsorbed molecules and amplifies the Raman signal through the chemical enhancement mechanism in SERS. By the fitting deconvolution and quantitative analysis, the observed SERS enhancement can be attributed to contributions from both MoO_x and defective MoS_2 (including sulfur vacancies and potentially 1T phase changes). The lower binding energy features reflecting increased defect density and metallic character relate to defective MoS_2, whereas the higher binding energy peaks indicate the presence of MoO_x species. These distinctions allow to separate the SERS contributions based on chemical state changes identified via XPS.

All these findings are in agreement with UV-Vis and Raman spectra, suggesting the presence of defective molybdenum oxides (MoO_x), which are also considered SERS-active oxide semiconductors [38]. These oxides contribute to the CM, controlled by defect density, leading to energy levels that align with those of the probe molecule, thereby facilitating charge transfer phenomena. At support of this, Zheng et al. demonstrated that thermal treatment of MoS_2 induces partial oxidation via oxygen substitution at sulfur sites, creating defect states that significantly enhance the chemical contribution to SERS, improving sensitivity by several orders of magnitude [9]. Yin et al. observed that the 1T phase of MoS_2 dramatically enhances the SERS response of copper phthalocyanine via substrate-analyte charge transfer, while pristine MoS_2 exhibited weak and inefficient charge transfer, leading to low SERS signals [33].

Pristine MoS_2 and laser-modified samples were therefore employed as SERS substrates to investigate the effect of defect introduction into the MoS_2 structure. SERS measurements were performed on MoS_2 substrates subjected to different laser irradiation times to assess how laser-induced modifications enhance their SERS performance for detecting adsorbed 4-MBA.

Figure 6a shows the SERS spectra of 4-MBA (10^{-4} M) adsorbed on MoS_2 substrates irradiated for 0, 5, 10, and 15 min. The spectra collected on pristine MoS_2 are nearly flat, confirming that the unmodified material is not an efficient SERS substrate. In contrast, laser-modified MoS_2 displays a progressive increase in SERS signal intensity with increasing irradiation time, demonstrating that laser exposure plays a crucial role in activating the SERS response. The spectra of irradiated samples show the characteristic 4-MBA vibrational bands at 1078 cm^{-1} and 1595 cm^{-1}, corresponding to the in-plane δ(CH) and aromatic ν(CC) stretching modes, respectively [39]. The gradual intensification of these peaks as irradiation time increases clearly indicates that laser modification enhances the adsorption of 4-MBA molecules and activates a chemical enhancement mechanism.

As discussed in previous sections, XPS and Raman data revealed that laser irradiation induces a high density of sulfur vacancies and other structural defects in MoS_2, along with a partial conversion from the semiconductor

2H phase to the metallic 1T phase, introducing new states in the electronic band structure. As discussed previously, these states may facilitate alignment between the MoS_2 electronic levels and the HOMO-LUMO levels of 4-MBA, enabling charge transfer under laser excitation. PL measurements further support this hypothesis, as the quenching of the intrinsic MoS_2 emission in the presence of 4-MBA confirms the electronic coupling between the substrate, the analyte, and the excitation wavelength.

Previous works report the role of defects, and 1T phase to improve the SERS performance of MoS_2. Zheng et al. demonstrated that thermal treatment of MoS_2 promotes partial oxidation and oxygen substitution at sulfur sites, leading to the formation of defect states that significantly increase the chemical enhancement contribution, boosting SERS sensitivity by several orders of magnitude [9]. Yin et al. reported that the metallic 1T phase of MoS_2 dramatically enhances the SERS response of copper phthalocyanine, attributing the effect to efficient substrate-analyte charge transfer, whereas pristine 2H-MoS_2 exhibited negligible enhancement [33].

Among the investigated samples, the substrate irradiated for 15 min exhibited the strongest enhancement and was therefore selected to study the detection capability over a range of 4-MBA concentrations (10^{-3}–10^{-6} M), as shown in Figure 6b. At higher concentrations (10^{-3} and 10^{-4} M), the spectra show intense bands at 1078 and 1595 cm^{-1}, along with weaker secondary features, indicating strong signal amplification. When the concentration decreases to 10^{-5} M, the two main peaks remain clearly visible, while at 10^{-6} M, they are still detectable but close to the noise level, suggesting that this concentration represents the detection limit of the system.

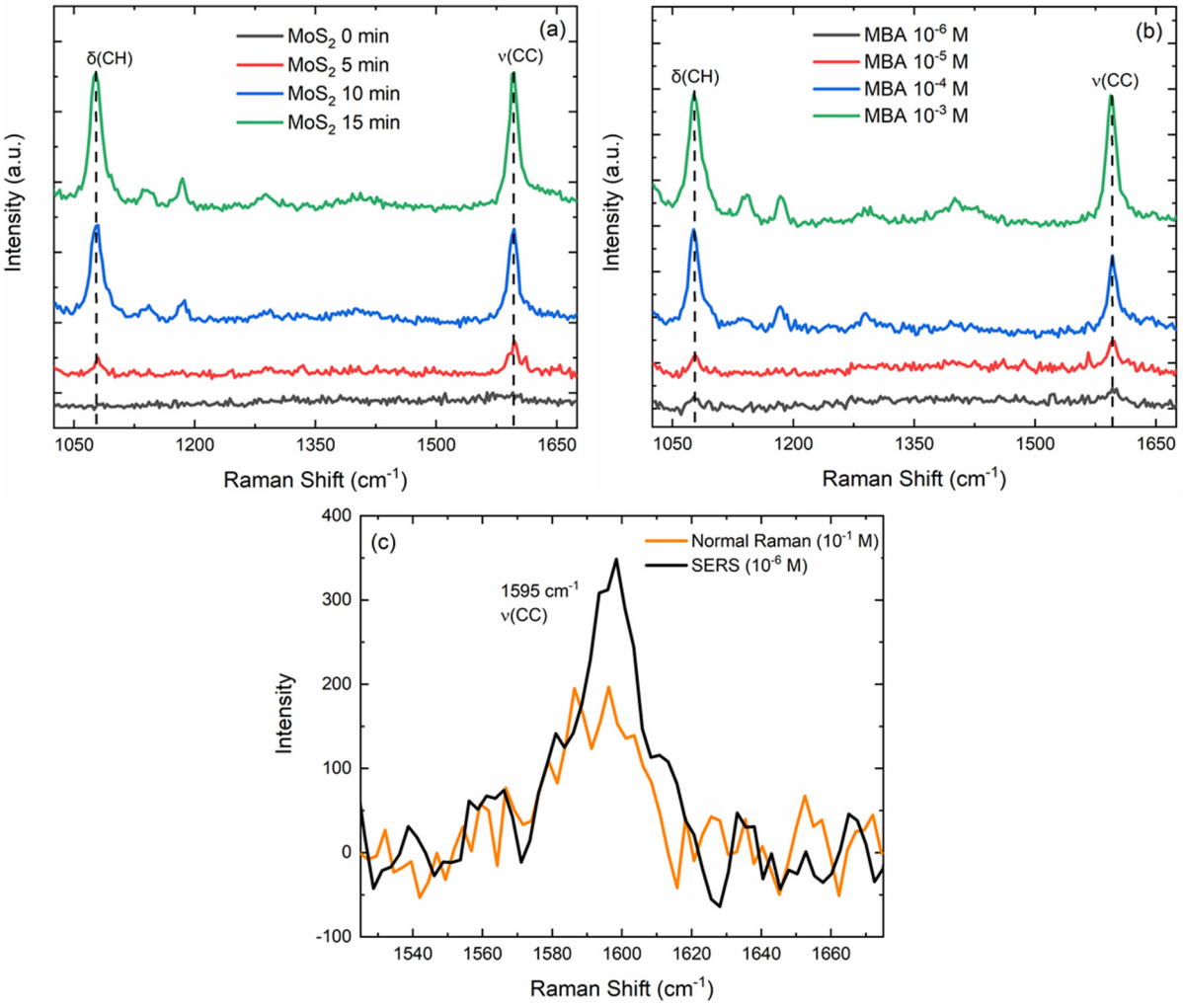

Figure 6. SERS spectra vs irradiation time of 4-MBA 10^{-4} M (**a**) and at different 4-MBA concentration for 15 min laser-modified MoS_2 (**b**). SERS spectra (ν(CC) vibrational mode) of 4-MBA 10^{-6} M on 15 min laser-modified MoS_2 vs Normal Raman of a 4-MBA 10^{-1} M solution (**c**).

To quantify the enhancement of the Raman scattering cross-section of the analyte, the Enhancement Factor (EF) is commonly employed and can be calculated in various ways depending on the specific information to extract. As reported by Le Ru et al., a facile approach, particularly useful for many analytical applications, focuses on evaluating how much stronger the SERS signal is expected to be compared to the Normal Raman signal under

identical experimental conditions [40]. According to this approach, the so-called Analytical Enhancement Factor (AEF) can be calculated as follows:

$$AEF = \frac{I_{SERS}/C_{SERS}}{I_{NR}/C_{NR}}$$

where I_{SERS} and I_{NR} represent the signal intensities obtained from the SERS and Normal Raman measurements, respectively, while C_{SERS} and C_{NR} correspond to the concentrations of the probe molecule in the SERS and normal Raman solutions.

To determine the AEF, we compared the signal intensities at 1595 cm^{-1} corresponding to the ν(CC) vibrational mode of 4-MBA. In Figure S1 (Supporting Information), the red trace represents the SERS spectrum, in the ν(CC) range, obtained using a laser-modified MoS_2 substrate interacting with a 10^{-6} M 4-MBA solution, while the black trace corresponds to the Normal Raman spectrum of a 10^{-1} M 4-MBA solution. From the measured signal intensities and their respective concentrations, an AEF value of 1.77×10^5 was derived.

The measured AEF for laser-modified MoS_2 falls within the range reported for defect-rich or partially oxidized MoS_2 and is consistent with literature values around 10^5 for chemically modified surfaces ($MoS_{2-x}/MoS_{2-x}O_x$) [41,42]. This AEF is 2–3 orders of magnitude larger than typical values reported for pristine 2H-MoS_2 [43], supporting the interpretation that pulsed-laser treatment induces sulfur vacancies, partial oxidation, and a partial 2H → 1T phase conversion; these changes increase substrate-adsorbate charge transfer and thereby enhance the chemical SERS response. It should be noted that many literature studies use highly absorbing organic dyes (e.g., rhodamine 6G or crystal violet) as probe molecules; such dyes can produce resonance-Raman effects at common excitation wavelengths and therefore increase the apparent EF [44,45]. By contrast, 4-mercaptobenzoic acid (4-MBA) is non-resonant at 532 nm, so the reported AEF predominantly reflects charge-transfer (chemical) enhancement rather than resonance-assisted or plasmonic contributions.

To assess the uniformity of the SERS response, Figure 7a displays SERS spectra of 4-MBA (10^{-4} M) acquired from different regions of interest (ROI), labeled "1–9" in the SERS map (Figure 7b), obtained selecting the 1595 cm^{-1} stretching vibration of the C=C bond (bright regions). Spectra show signals of comparable intensity corresponding to the characteristic fingerprint of 4-MBA. This indicates that 4-MBA molecules are uniformly adsorbed onto the substrate surface and detectable via charge transfer phenomena.

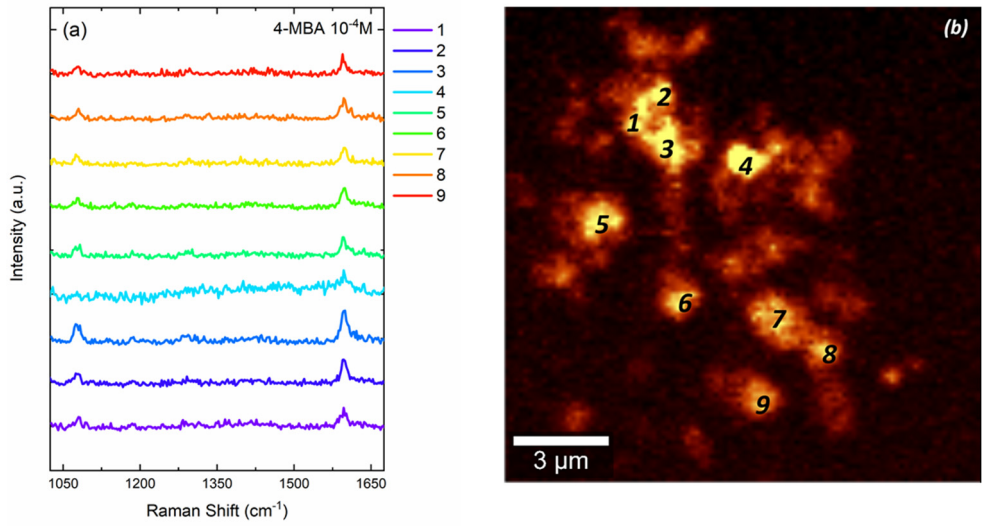

Figure 7. SERS spectra of 4-MBA 10^{-4} M onto 15 min laser-modified MoS_2 (**a**) extracted from SERS map of 1594 cm^{-1} 4-MBA signal ROI labelled as "1–9" (**b**).

5. Theoretical Modeling of Electronic and Interfacial Properties

To rationalize the experimental findings, first-principles density functional theory (DFT) simulations were performed using VASP. The models included pristine semiconducting 2H-MoS_2, sulfur-defective MoS_2 (MoS_2-VS), and metallic 1T-MoS_2, both in isolation and with adsorbed 4-MBA molecules. The projected density of states (PDOS) (Figure 8a,b) reveals that the valence and conduction bands of pristine 2H-MoS_2 are mainly composed of Mo *d* and S *p* orbitals, separated by a calculated band gap of approximately 1.7 eV.

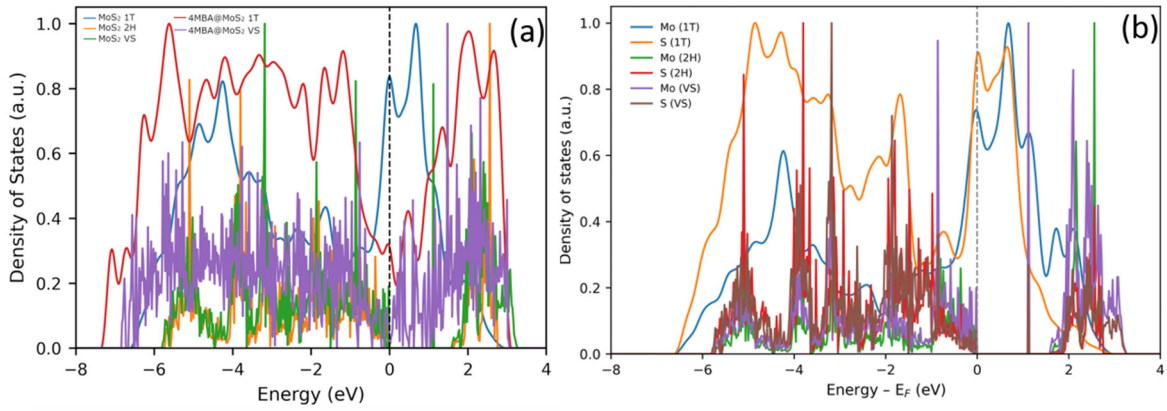

Figure 8. (**a**,**b**) Projected density of states (PDOS) for pristine and laser-modified MoS_2 surfaces and for 4-MBA adsorbed systems.

Upon creation of sulfur vacancies, new defect states appear near the Fermi level, narrowing the band gap and introducing localized donor levels. After 4-MBA adsorption, additional states emerge close to the conduction band edge, evidencing weak π–d coupling between the molecular orbitals and MoS_2 defect states. In the metallic 1T phase, the Mo *d* orbitals dominate around EF, producing a finite density of states at the Fermi level, as clearly shown in the PDOS comparison (Figure 8a). This metallic character is essential for enabling charge exchange with adsorbed molecules, consistent with the experimentally observed SERS activation after laser treatment. The calculated work functions (Φ) for the isolated substrates (Figure 9a) were 5.93 eV for 2H-MoS_2, 5.87 eV for MoS_2-VS, and −3.95 eV for metallic 1T-MoS_2. The adsorbed systems, 4-MBA@VS and 4-MBA@1T, exhibited comparable Φ values (−3.82 eV and −3.91 eV, respectively), indicating stabilization of the surface dipole upon adsorption. The substantial Φ reduction associated with the 1T phase highlights its enhanced electron-donor capability toward adsorbed species, which underlies the superior SERS activity of laser-irradiated samples. The vacuum-aligned energy-level diagram (Figure 9b) further clarifies this trend. The HOMO (−6.80 eV) and LUMO (−1.84 eV) of isolated 4-MBA lie deep within the band gap of 2H-MoS_2 (VBM = −17.1 eV, CBM = −15.5 eV), precluding charge transfer. In the defective MoS_2-VS phase, mid-gap states slightly improve the orbital overlap but remain energetically distant.

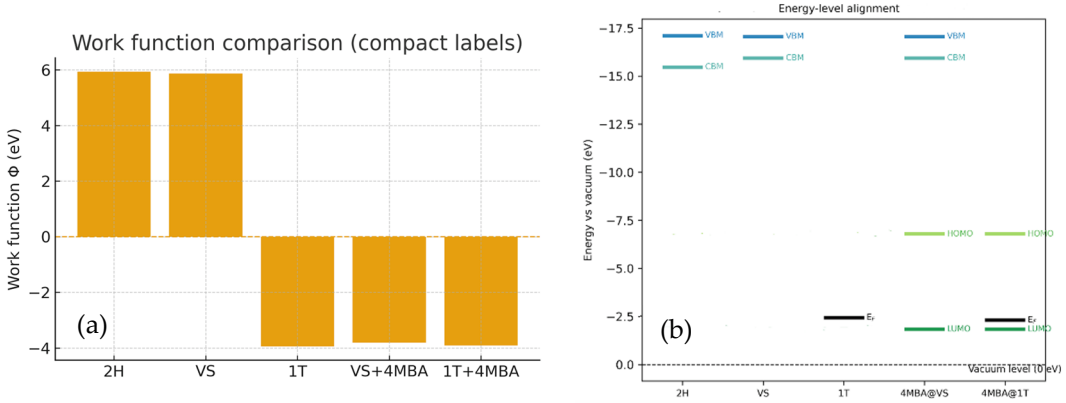

Figure 9. (**a**) Calculated work functions (Φ) for pristine, defected, and 1T MoS_2, and for 4-MBA adsorbed systems; (**b**) Vacuum potential alignment profiles derived from the electrostatic potential analysis.

Conversely, for metallic 1T-MoS_2, the Fermi level (−2.31 eV) approaches the 4-MBA frontier orbitals, making electron transfer feasible. The calculated alignment yields Δ(LUMO − EF) ≈ −8.8 eV and Δ(HOMO − EF) ≈ −13.8 eV for 4-MBA@1T, compared to Δ(LUMO − CBM) ≈ +13.6 eV for 4-MBA@2H, confirming that charge transfer from the MoS_2 substrate to the molecular LUMO is energetically favorable only for the metallic and defective systems. The integrated charge-density differences (Δρ) (Figure 10) provide a quantitative picture of the interfacial interaction. For 4-MBA@VS, moderate charge redistribution is observed, whereas 4-MBA@1T exhibits a much higher Δρ amplitude, indicating stronger electronic coupling and more efficient charge donation from MoS_2 to the molecule. This correlation supports a direct relationship between work-function reduction and charge-transfer intensity. The corresponding planar-averaged charge-density difference profiles Δρ(z) (Figure 11)

visualize this process, showing electron accumulation on the 4-MBA side and depletion near surface Mo atoms upon adsorption. The results confirm that the laser-induced structural transformation (2H → 1T) and defect creation (VS) synergistically promote a charge-transfer resonance mechanism responsible for the enhanced Raman response.

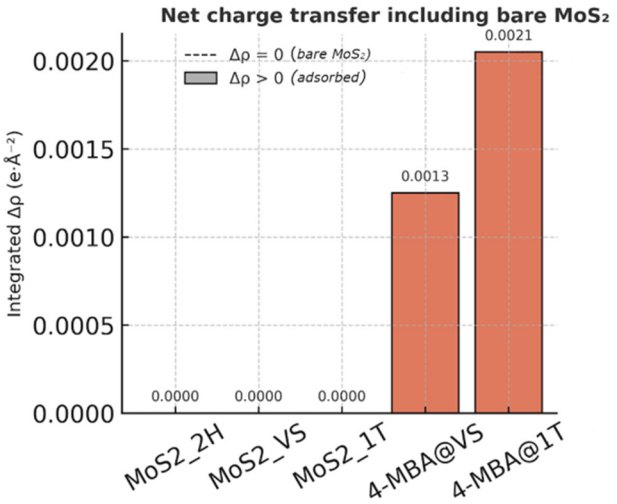

Figure 10. Integrated charge-density difference (Δρ) for bare and adsorbed MoS_2 systems.

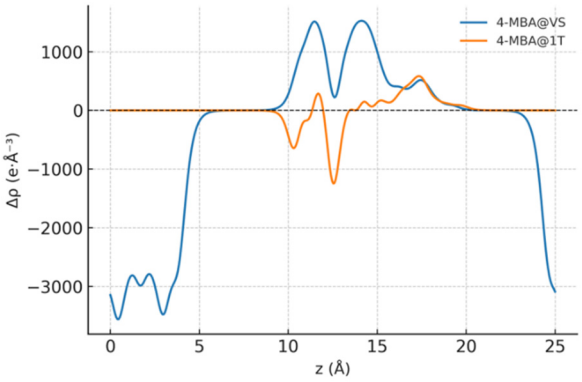

Figure 11. Charge-density difference profiles Δρ(z).

Overall, the combined theoretical and experimental evidence demonstrates that pulsed-laser irradiation induces a cascade of coupled modifications: (i) a phase transition from 2H to 1T MoS_2, increasing carrier density and metallic conductivity; (ii) defect generation, introducing donor-like states that act as adsorption and charge-transfer sites; and (iii) a pronounced work-function reduction, facilitating electron injection into the 4-MBA frontier orbitals. These effects collectively establish a non-plasmonic charge-transfer pathway that enhances the molecular polarizability under laser excitation. The observed SERS enhancement on laser-modified MoS_2 thus originates from a chemical (charge-transfer) mechanism, consistent with PL quenching, defect-related Raman bands, and the DFT-predicted lowering of Φ and favorable energy-level alignment.

6. Conclusions

This study demonstrates that PLIL is a versatile method for defect and phase engineering of MoS_2, enabling the fabrication of efficient noble metal-free substrates for SERS. Through morphological and spectroscopic characterization techniques, the effects of laser irradiation on the structure and properties of MoS_2 were systematically investigated. Electron microscopies revealed that increasing irradiation time promotes the structural reorganization of MoS_2 nanoflakes into larger structures, while optical absorption measurements showed a progressive disappearance of the excitonic transitions characteristic of the 2H phase and the appearance of new absorption bands associated with the formation of sulfur vacancies, sub-stoichiometric molybdenum oxides, and the metallic 1T phase. Raman spectroscopy confirmed these findings, showing the gradual emergence of vibrational modes typical of the 1T phase and oxide species, whereas XPS provided direct evidence of multiple molybdenum species, indicative of mixed-phase and defect-rich compositions.

The electronic and optical consequences of these transformations were further supported by PL analyses showing that the irradiated MoS_2 samples exhibited a weak emission band in the visible range, which was progressively quenched in the presence of 4-MBA, confirming charge-transfer interactions between the modified substrate and the adsorbed molecules.

In SERS experiments laser-induced modifications significantly enhance Raman signal intensity compared to pristine MoS_2, due to the coexistence of defective states and metallic domains providing a chemical enhancement, with a clear correlation between irradiation time, defect density, and SERS activity. The substrate irradiated for 15 min exhibited the highest enhancement, with an AEF of approximately 1.77×10^5 and a detection limit of 10^{-6} M. Moreover, mapping of the SERS response revealed a uniform spatial distribution of signal intensity, attesting to the repeatability and homogeneity of the laser-modified surfaces.

Theoretical calculations confirm that the laser-induced structural transformations and defect creation synergistically promote a charge-transfer resonance mechanism, consistent with experimental observations, including photoluminescence quenching and defect-related Raman features. The transition from the semiconducting 2H phase to the metallic 1T phase enhances carrier density and electrical conductivity, while the formation of sulfur vacancies introduces donor-like defect states that increase adsorption sites for probe molecules.

Therefore, this study highlights the critical role of phase transitions, defects, and work-function reduction in modulating charge transfer and provides new insights into the chemical mechanisms that govern SERS activity in laser-treated MoS_2. PLIL emerges as an alternative, fast and clean route for tailoring the electronic structure of two-dimensional semiconductor materials, producing MoS_2-based non-plasmonic SERS platforms potentially scalable into advanced chemical and biological detection systems.

Supplementary Materials

The additional data and information can be downloaded at: https://media.sciltp.com/articles/others/25121514 25422817/PS-25110011-SM-R1.pdf. Figure S1: Slabs modeled as a monolayer of MoS_2 metallic 1T (a) and with S vacancy sites (b) in presence of the adsorbate molecule, 4 mercaptobenzoic acid. Each model is reported with different space orientations.

Author Contributions

A.B.: Writing—original draft, Methodology, Investigation, Formal analysis. M.C.: Writing—original draft, Visualization, Validation, Supervision, Methodology, Investigation. V.S.: Writing—review & editing. G.F. Formal analysis, Investigation, Software. E.F.: Formal analysis, Investigation, Writing—review & editing. L.D.: Writing—review & editing, Supervision, Funding acquisition. G.C.: Writing—review & editing, Validation, Supervision, Resources, Funding acquisition. All authors have read and agreed to the published version of the manuscript.

Funding

The authors gratefully acknowledge the PON project Bionanotech Research and Innovation Tower (BRIT) financed by the Italian Ministry for Education, University and Research (MIUR). G.F. Indelli (BRIT) is acknowledged for the technical support. The author G.C. gratefully acknowledges PRIN PNRR 2022-ELATED. The author L.D. gratefully acknowledges PRIN 2022-LANCIA. The authors gratefully acknowledge support from the European Union (NextGeneration EU), through the MUR-PNRR project SAMOTHRACE (ECS00000022). The authors acknowledge: PRIDE: prog. n. RSH2A_000037, CUP F57G25000320006, NANOscience for Strategic applications from Green to Health (NANOSTRENGTH)-PIACERI 2024/2026.

Institutional Review Board Statement

Not applicable.

Informed Consent Statement

Not applicable.

Data Availability Statement

Data will be made available on request.

Conflicts of Interest

The authors declare no conflict of interest.

Use of AI and AI-Assisted Technologies

No AI tools were utilized for this paper.

References

1. Schmidt, M.M.; Brolo, A.G.; Lindquist, N.C. Single-Molecule Surface-Enhanced Raman Spectroscopy: Challenges, Opportunities, and Future Directions. *ACS Nano* **2024**, *18*, 25930–25938. https://doi.org/10.1021/ACSNANO.4C09483.
2. Matikainen, A.; Nuutinen, T.; Itkonen, T.; et al. Atmospheric oxidation and carbon contamination of silver and its effect on surface-enhanced Raman spectroscopy (SERS). *Sci. Rep.* **2016**, *6*, 37192. https://doi.org/10.1038/srep37192.
3. Zhao, X.; Wang, Y.; Liu, Y.; et al. Gradient Nanostructures and Machine Learning Synergy for Robust Quantitative Surface-Enhanced Raman Scattering. *Adv. Sci.* **2025**, *12*, 2501793. https://doi.org/10.1002/ADVS.202501793.
4. Ozdemir, R.; Hukum, K.O.; Usta, H.; et al. Organic and inorganic semiconducting materials-based SERS: Recent developments and future prospects. *J. Mater. Chem. C Mater.* **2024**, *12*, 15276–15309. https://doi.org/10.1039/D4TC02391A.
5. Krajczewski, J.; Michałowska, A.; Čtvrtlík, R.; et al. The battle for the future of SERS—TiN vs. Au thin films with the same morphology. *Appl. Surf. Sci.* **2023**, *618*, 156703. https://doi.org/10.1016/J.APSUSC.2023.156703.
6. Lan, L.; Gao, Y.; Fan, X.; et al. The origin of ultrasensitive SERS sensing beyond plasmonics. *Front. Phys.* **2021**, *16*, 43300. https://doi.org/10.1007/S11467-021-1047-Z.
7. Rani, D.; Patel, S.; Austeria, P.M.; et al. Surface-Enhanced Raman Spectroscopy (SERS) Chemical Enhancement in the Vibronically Coupled Langmuir Layer of Mixed Dichalcogenide 1T-MoSSe with Adsorbed R6G. *J. Phys. Chem. C* **2023**, *127*, 3131–3141. https://doi.org/10.1021/ACS.JPCC.2C08705.
8. Liu, H.; Li, Q.; Ma, Y.; et al. Study of charge transfer contribution in Surface-Enhanced Raman scattering (SERS) based on indium oxide nanoparticle substrates. *Spectrochim. Acta A Mol. Biomol. Spectrosc.* **2023**, *303*, 123168. https://doi.org/10.1016/J.SAA.2023.123168.
9. Zheng, Z.; Cong, S.; Gong, W.; et al. Semiconductor SERS enhancement enabled by oxygen incorporation. *Nat. Commun.* **2017**, *8*, 1993. https://doi.org/10.1038/S41467-017-02166-Z.
10. Zhang, M.; Wang, Y.; Ma, Y.; et al. Study of charge transfer effect in Surface-Enhanced Raman scattering (SERS) by using Antimony-doped tin oxide (ATO) nanoparticles as substrates with tunable optical band gaps and free charge carrier densities. *Spectrochim. Acta Part A Mol. Biomol. Spectrosc.* **2021**, *264*, 120288. https://doi.org/10.1016/J.SAA.2021.120288.
11. Gan, X.; Lee, L.Y.S.; Wong, K.Y.; et al. 2H/1T Phase Transition of Multilayer MoS_2 by Electrochemical Incorporation of S Vacancies. *ACS Appl. Energy Mater.* **2018**, *1*, 4754–4765. https://doi.org/10.1021/ACSAEM.8B00875.
12. Sun, S.; Zheng, J.; Sun, R.; et al. Defect-Rich Monolayer MoS_2 as a Universally Enhanced Substrate for Surface-Enhanced Raman Scattering. *Nanomaterials* **2022**, *12*, 896. https://doi.org/10.3390/NANO12060896.
13. Nair, P.R.; Ramirez, C.R.S.; Pinilla, M.A.G.; et al. Black titanium dioxide nanocolloids by laser irradiation in liquids for visible light photo-catalytic/electrochemical applications. *Appl. Surf. Sci.* **2023**, *623*, 157096. https://doi.org/10.1016/J.APSUSC.2023.157096.
14. Fazio, E.; Gökce, B.; De Giacomo, A.; et al. Nanoparticles Engineering by Pulsed Laser Ablation in Liquids: Concepts and Applications. *Nanomaterials* **2020**, *10*, 2317. https://doi.org/10.3390/NANO10112317.
15. Kresse, G.; Furthmüller, J. Efficient iterative schemes for ab initio total-energy calculations using a plane-wave basis set. *Phys. Rev. B* **1996**, *54*, 11169. https://doi.org/10.1103/PhysRevB.54.11169.
16. Kresse, G.; Joubert, D. From ultrasoft pseudopotentials to the projector augmented-wave method. *Phys. Rev. B* **1999**, *59*, 1758. https://doi.org/10.1103/PhysRevB.59.1758.
17. Perdew, J.P.; Burke, K.; Ernzerhof, M. Generalized Gradient Approximation Made Simple. *Phys. Rev. Lett.* **1996**, *77*, 3865. https://doi.org/10.1103/PhysRevLett.77.3865.
18. Dion, M.; Rydberg, H.; Schröder, E.; et al. Density Functional for General Geometries. *Phys. Rev. Lett.* **2004**, *92*, 246401. https://doi.org/10.1103/PhysRevLett.92.246401.
19. Román-Pérez, G.; Soler, J.M. Efficient Implementation of a van der Waals Density Functional: Application to Double-Wall Carbon Nanotubes. *Phys. Rev. Lett.* **2009**, *103*, 096102. https://doi.org/10.1103/PhysRevLett.103.096102.
20. Tang, W.; Sanville, E.; Henkelman, G. A grid-based Bader analysis algorithm without lattice bias. *J. Phys. Condens. Matter* **2009**, *21*, 084204. https://doi.org/10.1088/0953-8984/21/8/084204.
21. Luo, T.; Chen, X.; Wang, L.; et al. Green laser irradiation-stimulated fullerene-like MoS2 nanospheres for tribological applications. *Tribol. Int.* **2018**, *122*, 119–124. https://doi.org/10.1016/J.TRIBOINT.2018.02.040.
22. Compagnini, G.; Sinatra, M.G.; Messina, G.C.; et al. Monitoring the formation of inorganic fullerene-like MoS2 nanostructures by laser ablation in liquid environments. *Appl. Surf. Sci.* **2012**, *258*, 5672–5676. https://doi.org/10.1016/J.APSUSC.2012.02.053.

23. Ibrahim, K.; Novodchuk, I.; Mistry, K.; et al. Laser-Directed Assembly of Nanorods of 2D Materials. *Small* **2019**, *15*, 1904415. https://doi.org/10.1002/SMLL.201904415.
24. Zamharir, S.G.; Karimzadeh, R.; Aboutalebi, S.H. Laser-assisted tunable optical nonlinearity in liquid-phase exfoliated MoS2 dispersion. *Appl Phys A Mater Sci Process* **2018**, *124*, 692. https://doi.org/10.1007/S00339-018-2115-2.
25. Mosleh, A.; Alher, M.A.; Cousar, L.; et al. Transmission spectra of some transition metal dichalcogenides. II. Group VIA: trigonal prismatic coordination. *J. Phys. C: Solid. State Phys.* **1972**, *5*, 3540. https://doi.org/10.1088/0022-3719/5/24/016.
26. Kong, G.; Du, X.; Cai, X.; et al. Recycling Molybdenum Oxides from Waste Molybdenum Disilicides: Oxidation Experimental Study and Photocatalytic Properties. *Oxid. Met.* **2019**, *92*, 1–12. https://doi.org/10.1007/S11085-019-09909-X.
27. Stavrou, M.; Chazapis, N.; Nikoli, E.; et al. Crystalline Phase Effects on the Nonlinear Optical Response of MoS_2 and WS_2 Nanosheets. *ACS Appl. Nano Mater.* **2023**, *5*, 16674–16686. https://doi.org/10.1021/acsanm.2c03709.
28. Han, B.; Hu, Y.H. MoS_2 as a co-catalyst for photocatalytic hydrogen production from water. *Energy Sci. Eng.* **2016**, *4*, 285–304. https://doi.org/10.1002/ESE3.128.
29. Khan, Y.; Obaidulla, S.M.; Habib, M.R.; et al. Anomalous photoluminescence quenching in DIP/MoS2 van der Waals heterostructure: Strong charge transfer and a modified interface. *Appl. Surf. Sci.* **2020**, *530*, 147213. https://doi.org/10.1016/J.APSUSC.2020.147213.
30. Li, H.; Zhang, Q.; Yap, C.C.R.; et al. From Bulk to Monolayer MoS_2: Evolution of Raman Scattering. *Adv. Funct. Mater.* **2012**, *22*, 1385–1390. https://doi.org/10.1002/ADFM.201102111.
31. Chang, H.P.; Hofmann, M.; Hsieh, Y.P.; et al. Correlation of grain orientations and the thickness of gradient MoS_2 films. *RSC Adv.* **2021**, *11*, 34269–34274. https://doi.org/10.1039/D1RA05982C.
32. Ye, F.; Chang, D.; Ayub, A.; et al. Synthesis of Two-Dimensional Plasmonic Molybdenum Oxide Nanomaterials by Femtosecond Laser Irradiation. *Chem. Mater.* **2021**, *33*, 4510–4521. https://doi.org/10.1021/ACS.CHEMMATER.1C00732.
33. Yin, Y.; Miao, P.; Zhang, Y.; et al. Significantly Increased Raman Enhancement on MoX2 (X = S, Se) Monolayers upon Phase Transition. *Adv. Funct. Mater.* **2017**, *27*, 1606694. https://doi.org/10.1002/ADFM.201606694.
34. Li, B.; Jiang, L.; Li, X.; et al. Preparation of Monolayer MoS_2 Quantum Dots using Temporally Shaped Femtosecond Laser Ablation of Bulk MoS_2 Targets in Water. *Sci. Rep.* **2017**, *7*, 11182. https://doi.org/10.1038/S41598-017-10632-3.
35. Tran, H.N.; Park, S.; Wibowo, F.T.A.; et al. 17% Non-Fullerene Organic Solar Cells with Annealing-Free Aqueous MoO_x. *Adv. Sci.* **2020**, *7*, 2002395. https://doi.org/10.1002/ADVS.202002395.
36. Xu, Q.; Li, X.; Wu, L.; et al. Enlarged Interlayer Spacing of Marigold-Shaped 1T-MoS_2 with Sulfur Vacancies via Oxygen-Assisted Phosphorus Embedding for Rechargeable Zinc-Ion Batteries. *Nanomaterials* **2023**, *13*, 1185. https://doi.org/10.3390/NANO13071185.
37. Mouloua, D.; Rajput, N.S.; Lejeune, M.; et al. Giant Photodegradation Rate Enabled by Vertically Grown 1T/2H MoS_2 Catalyst on Top of Silver Nanoparticles. *Adv. Energy Sustain. Res.* **2024**, *5*, 2400213. https://doi.org/10.1002/AESR.202400213.
38. Gu, C.; Li, D.; Zeng, S.; et al. Synthesis and defect engineering of molybdenum oxides and their SERS applications. *Nanoscale* **2021**, *13*, 5620–5651. https://doi.org/10.1039/D0NR07779H.
39. Ho, C.H.; Lee, S. SERS and DFT investigation of the adsorption behavior of 4-mercaptobenzoic acid on silver colloids. *Colloids Surf. A Physicochem. Eng. Asp.* **2015**, *474*, 29–35. https://doi.org/10.1016/J.COLSURFA.2015.03.004.
40. Le Ru, E.C.; Etchegoin, P.G. Quantifying SERS enhancements. *MRS Bull.* **2013**, *38*, 631–640. https://doi.org/10.1557/MRS.2013.158.
41. Pramanik, A.; Gao, Y.; Gates, K.; et al. Giant Chemical and Excellent Synergistic Raman Enhancement from a 3D $MoS_{2-x}O_x$−Gold Nanoparticle Hybrid. *ACS Omega* **2019**, *4*, 11112–11118. https://doi.org/10.1021/acsomega.9b00866.
42. Yin, Y.; Li, C.; Yan, Y.; et al. MoS_2-Based Substrates for Surface-Enhanced Raman Scattering: Fundamentals, Progress and Perspective. *Coatings* **2022**, *12*, 360. https://doi.org/10.3390/COATINGS12030360.
43. Er, E.; Hou, H.-L.; Criado, A.; et al. High-Yield Preparation of Exfoliated 1T-MoS 2 with SERS Activity. *Chem. Mater.* **2019**, *31*, 5725–5734. https://doi.org/10.1021/acs.chemmater.9b01698.
44. Shim, S.; Stuart, C.M.; Mathies, R.A. Resonance Raman cross-sections and vibronic analysis of rhodamine 6G from broadband stimulated Raman spectroscopy. *Chemphyschem* **2008**, *9*, 697–699. https://doi.org/10.1002/CPHC.200700856.
45. Angeloni, L.; Smulevich, G.; Marzocchi, M.P. Resonance Raman spectrum of crystal violet. *J. Raman Spectrosc.* **1979**, *8*, 305–310. https://doi.org/10.1002/JRS.1250080603.